Tuning electrochemical and transport processes to achieve extreme performance and efficiency in solid oxide cells

ARTICLE

Tuning electrochemical and transport processes to achieve extreme performance and efficiency in solid oxide cells

Beom-Kyeong Park, Roberto Scipioni, Qian Zhang, Dalton Cox, Peter W. Voorhees, and Scott A. Barnett*

Solid oxide cells (SOCs) have important applications as fuel cells and electrolyzers. The application for storage of renewable electricity is also becoming increasingly relevant; however, it is difficult to meet stringent area-specific resistance (ASR) and long-term stability targets needed to achieve required efficiency and cost. Here we show a new SOC that utilizes a very thin Gd-doped Ceria (GDC)/Yttria-stabilized Zirconia (YSZ) bi-layer electrolyte, Ni–YSZ cell support with enhanced porosity, and electrode surface modification using PrO_x and GDC nanocatalysts to achieve unprecedented low ASR values < 0.1 Ωcm^2, fuel cell power density ~3 Wcm^{-2}, and electrolysis current density ~4 Acm^{-2} at 800 ^{o}C. Besides this exceptionally high performance, fuel cell and electrolysis life tests suggest very promising stability in fuel cell and steam electrolysis modes. Electrochemical impedance spectroscopy analysis done using a novel impedance subtraction method shows how rate-limiting electrode processes are impacted by the new SOC materials and design.

1. Introduction

Solid oxide cells (SOCs) have been developed as high efficiency fuel cells and electrolyzers,[1-4] for production of pure oxygen,[1,5] CO,[6] and for augmenting bio-mass fuel production.[1] Growing concerns regarding climate change, and the realization that long-term storage is needed to augment intermittent renewable energy sources, have driven growing interest in the application of reversible SOCs for long-term electricity storage.[7-11] Although SOCs work very well with hydrogen, the most widely-discussed storage medium, technical challenges remain for developing the hydrogen storage and distribution infrastructure.[12,13] Thus, it is worth noting that SOCs are quite amenable to alternative storage media; co-electrolysis of CO_2 and H_2O SOCs can yield syngas for production of various hydrocarbon or alcohol fuels,[1,2] or directly produce a methane-rich product with high efficiency.[9,10]

Much of the SOC R&D has focused on reducing costs and improving stability, typically by reducing operating temperature and increasing power density. However, for the energy storage application, reducing cell and stack area-specific resistance is especially important.[10,14] This latter point can be elucidated by considering the round-trip voltage efficiency η, which provides an upper limit on the efficiency that can be achieved by a reversible cell operating part time as an electrolyzer at voltage V_{EL} and part time as a fuel cell at voltage V_{FC}. In order to provide a simple illustration, we assume a linear current-voltage characteristic with cell area-specific resistance R_{AS} (as widely

observed for SOCs)[15–18] with operation time and current density j equal in both modes, giving

$$\eta = \frac{V_{FC}}{V_{EL}} = \frac{V_{OC} - jR_{AS}}{V_{OC} + jR_{AS}} \qquad (1)$$

where V_{OC} is the open-circuit voltage. For example, to reach η ~70 %, as needed to be competitive with other storage methods,[9,19] R_{AS} ~0.15 Ωcm^2 is needed assuming reasonable values of j = 1 Acm^{-2} and V_{OC} = 0.9 V. Even lower R_{AS} values are desirable, because stack resistance values are typically higher than single-cell values and since system-level storage efficiencies will be lower than this ideal cell-voltage efficiency due to, e.g., steam/fuel utilization considerations.[11,20] Note also that the lower limit of V_{EL}, and hence the maximum η, may also be limited by thermal neutrality considerations.[10]

There has been considerable R&D activity in improving SOC performance. Nonetheless, typical reported R_{AS} values are ~0.3 Ωcm^2, and the lowest reported R_{AS}, ~0.12 Ωcm^2, barely meets the criterion noted above.[21-24] Higher SOC performance can often be achieved by increasing operating temperature, but there are significant limitations: cell materials or microstructures are often not compatible with higher temperatures,[3,23,25-28] mass transport may limit high temperature performance, and some electrolyte types (e.g. Ceria-based or protonic electrolytes) develop significant electronic conductivity that will compromise efficiency.[22,24,29-33] Finally, in most cases these new SOCs have not undergone sufficient life testing to prove the long-term stability of their R_{AS} values.

Here we describe a new SOC approach that pushes the limits of the R_{AS} values that can be achieved. All of the main cell components are improved to produce a novel cell with extremely low R_{AS}, 0.075 Ωcm^2 at 800 ^{o}C, with corresponding

Department of Materials Science and Engineering, Northwestern University, Evanston, Illinois 60208, USA. E-mail: s-barnett@northwestern.edu

maximum fuel cell power densities exceeding 3 Wcm^{-2} and electrolysis current densities at 1.3 V exceeding 4 Acm^{-2}. To gain fundamental insights into how the cell improvements affect performance, a novel impedance spectra subtraction method is used to help determine the rate-limiting electrochemical processes. The infiltration-enhanced electrodes are found to lower activation polarization losses, the ultra-thin bi-layer electrolyte is found to reduce ohmic losses, and increased support porosity is found to be a key factor for reducing concentration polarization losses. 1000-h life tests at relatively high electrolysis and fuel-cell current densities show promisingly good stability.

2. Results & discussion

The results presented below show how changes to each cell component affect performance and how they impact fundamental cell processes. The baseline SOC is a modified version of a typical "anode-supported" SOC, as previously reported to provide very good electrochemical performance.[16,18] The modification is the reduced-temperature firing procedure that yields a YSZ electrolyte with a dense GDC barrier layer without deleterious interdiffusion, along with decreased feature size and increased three-phase boundary density in the Ni–YSZ fuel electrode.[16] The other modification is a recently-reported high-performance and high stability oxygen electrode, Sr(Ti$_{0.3}$Fe$_{0.63}$Co$_{0.07}$)O$_{3-\delta}$ (STFC).[18] The following successive improvements were made: (1) decreasing the thickness of the electrolyte from ~10 to ~2.5 μm (termed the "Baseline" cell), (2) infiltrating PrO$_x$ catalyst into the oxygen electrode (termed the "PrO$_x$" cell),[34] (3) infiltrating GDC catalyst into the fuel electrode (termed the "PrO$_x$/GDC" cell),[35] and (4) increasing the support porosity (termed the "PrO$_x$/GDC/Pore+" cell). The electrode materials in each cell are summarized in Table S1.

2.1 Effect of modifications on SOC performance

A key factor in these cells is the relatively small electrolyte and barrier layer thickness. The SEM images in Figs. 1(a) (and S1) and SEM–EDS chemical mapping image in Fig. 1(b) show a typical PrO$_x$/GDC cell. The electrolyte is reasonably dense with ~1.5 μm thick YSZ and ~1 μm thick GDC layers. Although there is no GDC/YSZ interdiffusion measurable by EDS due to its spatial resolution limits, prior work has revealed an ~ 0.5 μm thick interdiffusion zone for the present co-firing conditions.[16] Electrolyte resistance values estimated from EIS measurements (Fig. S2) were reduced by ~45–60 % compared to a typical SOC made with a ~8 μm-thick GDC/YSZ electrolyte.[16,35] This reduction is important for maintaining low ohmic resistance R_Ω, e.g., < 0.23 Ωcm^2 at temperature $\geq$ 550 °C. Figs. 1(c) and (d) exhibit magnified views of the porous electrodes, where PrO$_x$ nanoparticles in STFC and GDC nanoparticles in Ni–YSZ are seen to be present after cell testing.
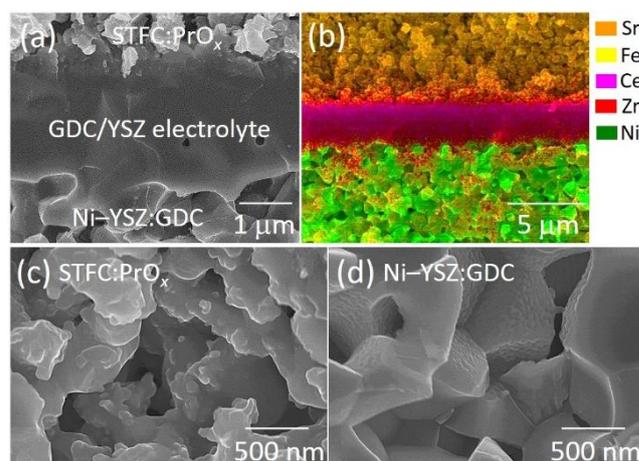

Fig. 1 (a) Fracture cross-sectional SEM image of the PrO$_x$/GDC cell after electrochemical characterization. (b) SEM–EDS elemental maps for Sr, Fe, Ce, Zr, and Ni from a fracture cross section of the PrO$_x$/GDC cell, after a 1000-h life test at 600 °C. Higher-magnification cross-sectional SEM images of the (c) oxygen and (d) fuel electrodes of the PrO$_x$/GDC cell after electrochemical characterization.

Fig. 2 shows that the Baseline cell performance is already very good, e.g., maximum power density of nearly 2 Wcm^{-2} at 750 °C, but modification yields substantial improvements. PrO$_x$ is added to the STFC by single-step infiltration yielding a power density increase as shown in Fig. 2 (also see Figs. S3 and S4), in agreement with recent results showing substantial oxygen electrode performance enhancement.[34,36] Single-step infiltration of GDC into Ni–YSZ results in further performance improvements, in agreement with recent results.[35,37] The increases in power density resulting from the infiltrations are most pronounced at lower cell operating temperature, i.e., at 550 °C in Fig. 2.

At the higher temperatures in Fig. 2, there is a clear indication of mass transport limitation at high current density. This suggests that gas diffusion through the relatively thick Ni–YSZ support layer limits cell performance. Thus, a further cell improvement is made by increasing the support porosity via additional graphite pore former. Figs. 2 and S5 show that this tailored support eliminates the limiting current, and thereby improves cell performance, reaching 2.9 Wcm^{-2} at 750 °C, ~1.7 Wcm^{-2} at 650 °C, and ~0.5 Wcm^{-2} at 550 °C. The effect is not so pronounced at 550 °C (see also Fig. S6), because the current density values are low enough to avoid most concentration polarization. Stereological analysis of the post-test cell SEM images (Fig. S7) was used to show the effect of the additional graphite pore former.[38] The porosity ε increased from ~0.35 to 0.55 due to the pore former, with a resulting decrease in pore tortuosity τ from ~1.51 to 1.29. The effective gas diffusivity was thus increased by a factor ε/τ = 1.84, consistent with the improved cell performance in Fig. 2.
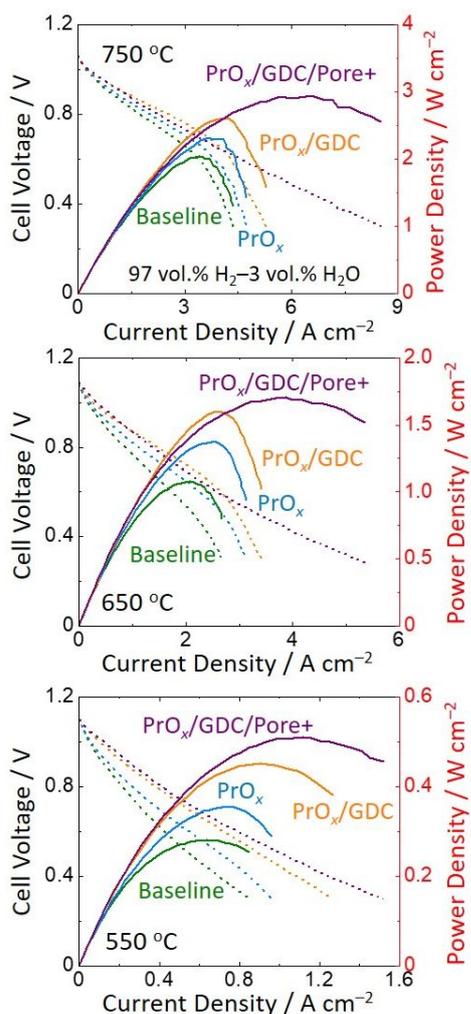
Fig. 2 Cell voltage and power density versus current density for the Baseline, PrO_x, PrO_x/GDC, and PrO_x/GDC/Pore+ cells measured at 550, 650, and 750 °C in 97 vol.% H_2–3 vol.% H_2O and air.

The PrO_x/GDC and PrO_x/GDC/Pore+ cells were also tested in electrolysis mode in a typical 50 vol.% H_2–50 vol.% H_2O fuel mixture. Fig. 3 presents the resultant j–V curves in both fuel cell and electrolysis modes (Fig. S8 shows the corresponding impedance spectra). The PrO_x/GDC cell shows limiting current in fuel cell mode at lower currents than shown in Fig. 2, due to the lower content of the diffusing species, H_2. The limiting current in electrolysis mode is smaller than in fuel cell mode, presumably due to the higher atomic mass and hence lower diffusivity of the diffusing species, H_2O. The PrO_x/GDC/Pore+ cell shows a more linear j–V dependence with no evidence of concentration polarization; as a result, fuel cell maximum power density and electrolysis current density values are substantially increased, especially at higher operating temperatures (Fig. S9 plots the maximum fuel cell power densities and electrolysis current densities at 1.3 V). The electrolysis current densities especially benefit, reaching values of 4.25 Acm⁻² at 800 °C, 2.9 Acm⁻² at 700 °C, and 1.25 Acm⁻² at 600 °C.
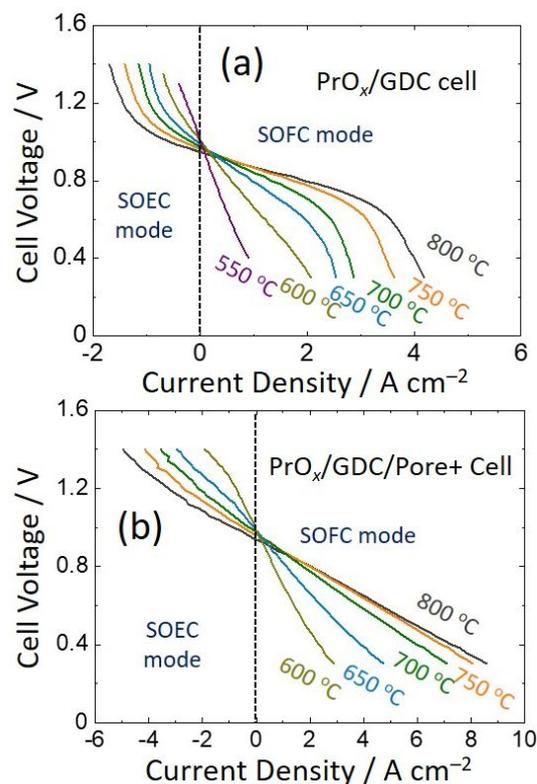

Fig. 3 Cell voltage versus current density for the (a) PrO_x/GDC and (b) PrO_x/GDC/Pore+ cells measured at 600–800 °C in 50 vol.% H_2–50 vol.% H_2O and air.

Fig. 4 provides a comparison of the above results for the PrO_x/GDC/Pore+ cell compared with literature data for area-specific resistance,[9,16,18,30-33,39] maximum fuel cell power density,[18,21-24,29,40] and electrolysis current density at 1.3 V.[9,16,18,30-33,39] Fig. 4(a) shows that the PrO_x/GDC/Pore+ cell produces the lowest reported R_{AS} over the entire temperature range, and is < 0.15 Ωcm² for temperatures > 650 °C. Fig. 4(b) shows the ideal voltage efficiency η, which exceeds 70 % at 1 Acm⁻² even at 650 °C, and gradually increases with increasing temperature. Note that some of the literature results in Fig. 4 are for ceria-based electrolytes, where the mixed conductivity would lead to prohibitively low η values in energy storage applications, even if they may be feasible for fuel cell applications. For the protonic electrolyte-based cells in Fig. 4, protonic electrolyte mixed conductivity tends to increase with increasing temperature, a factor that will limit η values,[24] especially for cells operated much above 600 °C. Regarding fuel cell power density and electrolysis current density, the present cell provides performance slightly lower than the best cells at lower temperature, but substantially exceeds the prior cell performance at ≥ 700 °C. The highest fuel cell power density value, 3.18 Wcm⁻², exceeds the best reported value of 2.4 Wcm⁻².[29] Similarly, the highest electrolysis current density of 4.25 Acm⁻² easily exceed the best prior value of 3.2 Acm⁻².[18]
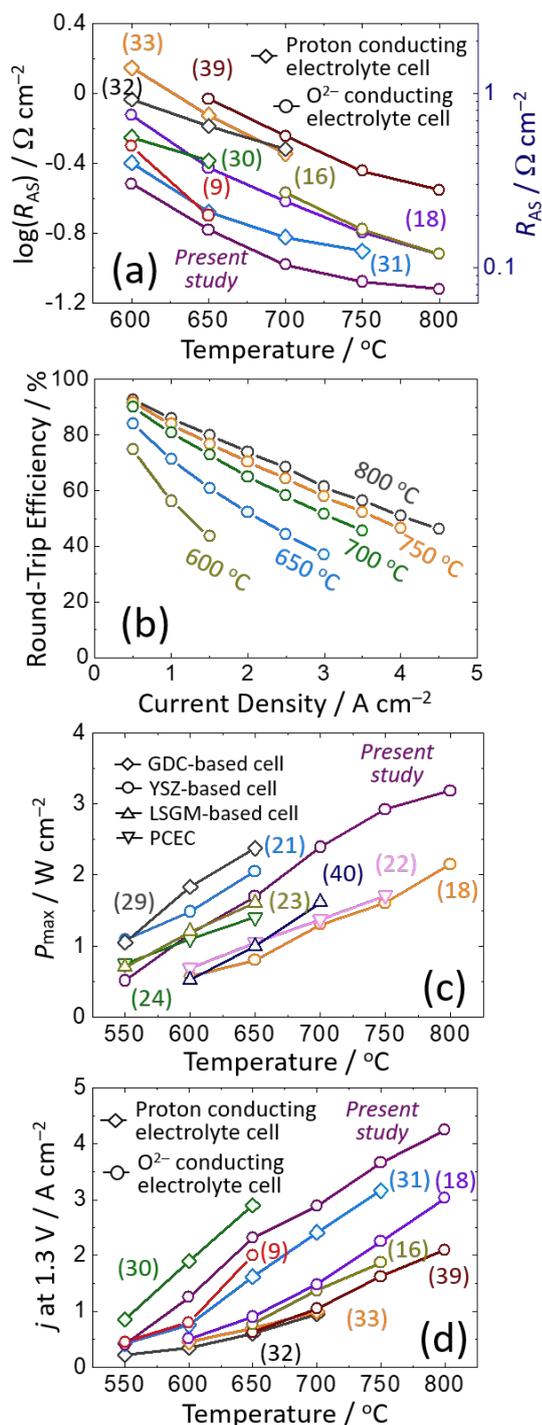
Fig. 4 Comparison of the present PrO$_x$/GDC/Pore+ cell performance with high performing cells in the literature: (a) cell area-specific resistances (R_{AS}); (c) maximum fuel-cell power densities P_{max}; and (d) electrolysis mode current densities (j) at 1.3 V. (b) shows round-trip voltage efficiency ($\eta = V_{FC}/V_{EL}$) vs. current density at different temperatures from the data for the PrO$_x$/GDC/Pore+ cell in 50 vol.% H$_2$–50 vol.% H$_2$O and air shown in Fig. 3(b).

2.2 Electrochemical Analysis

Figs. 5(a) and (b) illustrate Nyquist and Bode plots of the impedance spectra for all the cells, measured in 97 vol.% H$_2$–3 vol.% H$_2$O and air at 600 °C (other conditions are shown in Fig. S4). The Nyquist plots show that the cell polarization resistance decreases from the Baseline cell to PrO$_x$ to PrO$_x$/GDC to PrO$_x$/GDC/Pore+, in agreement with the above current-voltage results. The Bode plots show that all the cells have responses over a wide range of frequencies, that are strongly overlapped. Although DRT analysis can be used to help separate the different responses,[34,35] overlaps between the fuel and oxygen electrodes often make it difficult to fully separate all the processes. Here we use a unique impedance subtraction method in order to isolate the effects of specific cell changes on electrode processes, and thereby better understand the present high-performance SOC electrodes. This method was used previously to examine effects of different cell operating conditions,[41] but this is the first case, to our knowledge, where different cells are compared.
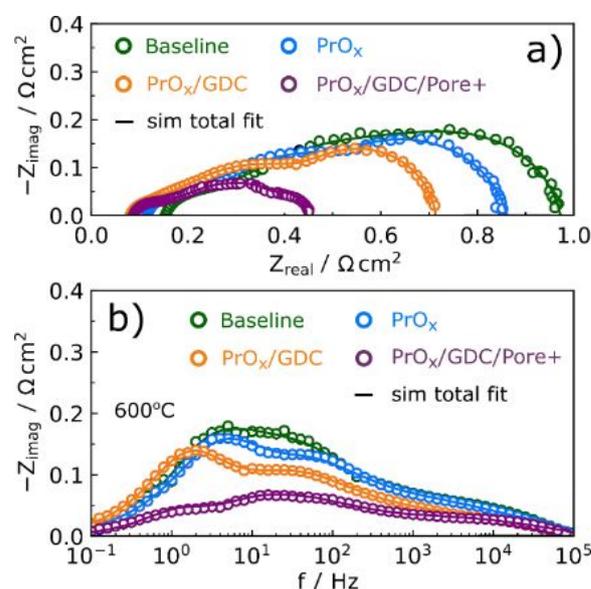

Fig. 5 (a) Nyquist and (b) Bode plots of the impedance spectra for the Baseline, PrO$_x$, PrO$_x$/GDC, and PrO$_x$/GDC/Pore+ cells measured at 600 °C in 97 vol.% H$_2$–3 vol.% H$_2$O and air. Best fits to the data, using the model described in the text, are shown as solid lines.

Fig. 6 shows the imaginary impedance difference (ΔZ_{im}) spectra – negative changes indicate a reduction in the impedance. The differences are generally more pronounced at lower temperatures where the electrode resistances are larger. Fig. 6(a) shows the effect of PrO$_x$ infiltration (subtraction of the baseline from the PrO$_x$ cell spectrum), a reduction in the impedance in the mid- and low-frequency regions (below 1 kHz); this agrees with a prior report showing that PrO$_x$ primarily impacts these frequencies, and associated them with improved oxygen vacancy transport and faster gas-solid interactions, respectively.[34] Fig. 6(b) shows the effect of GDC infiltration (subtraction of the PrO$_x$ from the PrO$_x$/GDC cell spectrum), a reduction of Z in the high- and mid-frequency regions (above 3 Hz), but an increase at low frequency (below 3 Hz). These

ARTICLE

changes are consistent with prior reports of the effect of GDC infiltration[35,37] showing that it reduces the fuel electrode interfacial reaction and oxygen ion transport resistances. On the other hand, the increase at low frequency reflects an increase in gas diffusion resistance due to a reduction in electrode pore volume by the infiltrated GDC. Fig. 6(c) shows that increasing support porosity (subtraction of the PrO$_x$/GDC from the PrO$_x$/GDC/Pore+ cell spectrum), reduces the low frequency gas diffusion resistance.
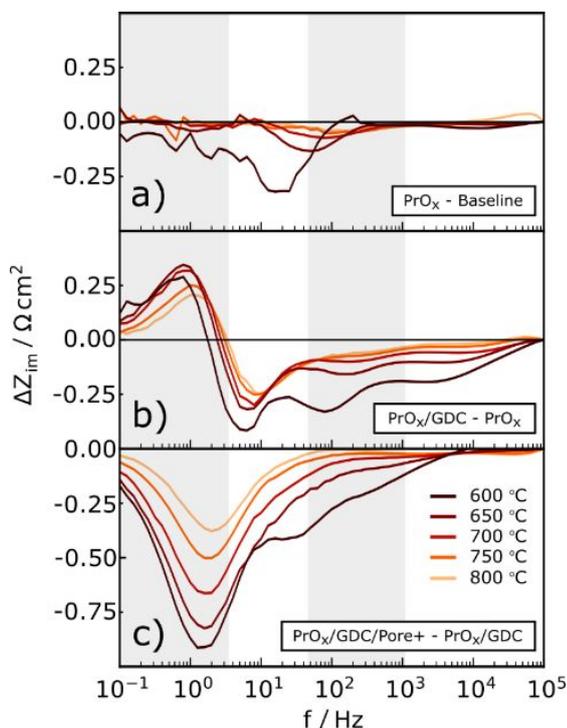

Fig. 6 ΔZ_{im} spectra obtained from the EIS data of cell baseline showing the changes caused by (a) PrO$_x$ infiltration, (b) GDC infiltration, and (c) increasing support porosity.

Based on the responses observed in the subtraction results and the responses normally present in solid oxide cells,[34,42] a simple equivalent circuit model (see Fig. S10) is developed that includes an RQ element for the high frequency a simplified transmission line for the mid-frequency and a general finite length Warburg W_{GFL} for the fuel diffusion in the support.[34,35] Although the resulting fits to the data in Fig. 5 are good, the model clearly simplifies the actual cells responses; some of the elements are a superposition of responses from the two electrodes, as observed previously for SOCs.[43] However, one response in these cells has a straightforward interpretation – the low-frequency response corresponds to gas diffusion in the thick fuel-electrode support. The diffusion coefficient D obtained from the fits increases from ~6×10^{-3} to ~1.1×10^{-2} by increasing support porosity. This agrees well with the increase by a factor $\varepsilon/\tau = 1.84$ for the modified support based on stereology result discussed above. This increase in effective diffusivity yields the substantial increase in limiting currents in Fig. 3.

2.3 Long-term stability

The operating stability of SOCs is critical for practical applications, and is of particular interest in the present cells for a few reasons: (*i*) there are known question regarding the stability of infiltrated nanocatalysts due to particle coarsening at high temperatures;[28,44,45] (*ii*) the electrolyte is unusually thin; and (*iii*) electrolysis operation at high current densities is often observed to cause SOC degradation. Thus, the cells were life tested under a range of conditions.

Fig. 7(a) presents the current density versus time during fuel cell operation at 0.7 V for the PrO$_x$/GDC cell at 600 ^{o}C and the PrO$_x$/GDC/Pore+ cell at 750 ^{o}C. At 600 ^{o}C, the current is essentially stable – the small decrease (~1 %) is within the measurement accuracy of the life test. At 750 ^{o}C, the current density decreases by 28 % during the first ~300 h, but then stabilizes at 2.54 A cm^{-2} (maximum power density of 2.15 W cm^{-2}, Fig. S11(a)). Over the final ~700 h of the test, the current density varies with no clear trend, but there is no suggestion of serious long-term degradation. The EIS data (see Figs. S11(b) and S12) show that the early-stage cell degradation at 750 ^{o}C is mainly due to an R_p increase at ~10^3 to 10^4 Hz – the impedance difference data in Fig. 6 suggests that this degradation arises from the GDC-infiltrated Ni–YSZ. This may be explained by prior work suggesting that coarsening of the GDC degrades electrode performance during the early stages of cell operation.[37] While PrO$_x$ is also known to coarsen and degrade at elevated temperature,[34] the resistance of the STFC electrode is very low at 750 ^{o}C such that it will have little impact on cell performance.[18] There was little apparent increase in ohmic resistance in either life test. Overall, demonstration of stable fuel cell operation over 1000 h at high power density – 1.0 Wcm^{-2} at 0.7 V and 600 ^{o}C, and 1.8 Wcm^{-2} at 0.7 V and 750 ^{o}C – is very promising.

Fig. 7(b) shows voltage versus time for a PrO$_x$/GDC/Pore+ cell life tested in electrolysis mode in 50 vol.% H$_2$O at 700 ^{o}C. The cell voltage increases rapidly over the first ~50 h of operation, more gradually during the first 500 h, and then remains relatively stable (18 mV/kh degradation rate) over the last 500 h. Similar early-stage degradation followed by stabilization has been observed previously during electrolysis.[37] EIS data taken during and after the life test (Figs. S13) shows that R_Ω remains fairly stable while R_p increases during the first 500 h, consistent with the voltage increase shown in Fig. 7(b). SEM–EDS images taken after the life tests (Fig. S14) showed no obvious changes from the pre-test images, further supporting the good fuel cell stability.

The observation of stable electrolysis operation at such a high current density is unusual – most prior reports of electrolysis operation at > 1 Acm^{-2} show significant degradation.[8,37,46-48] Such degradation has been associated with extremely high oxygen partial pressure at the oxygen electrode and low oxygen partial pressure at the fuel electrode.[46,47] Here we present results of a mathematical electrolyte model (see ESI) that has been used to quantitatively predict oxygen electrode degradation and explain fuel electrode degradation.[46] Fig. 7(c) shows the calculated oxygen partial pressure (P_{O_2}) *vs.* position

in the electrolyte, using input values from the cell life tested in Fig. 7(b). The P_{O_2} value at the oxygen electrode side remains moderate, well below the values (~10^4 atm) that cause fracture.[46] The P_{O_2} value at the fuel electrode side are as low as 10^{-28} atm, not as low as values expected to cause electrolyte or electrode damage.[37,46-49] Note that the moderate P_{O_2} values are largely the result of low electrode R_p values in the PrO$_x$/GDC/Pore+ cell, which yield relatively low electrode overpotentials. SEM–EDS images taken after the life tests (Fig. S14) showed evidence of the microstructural degradation often observed during electrolysis,[37,47-49] further supporting the good stability.
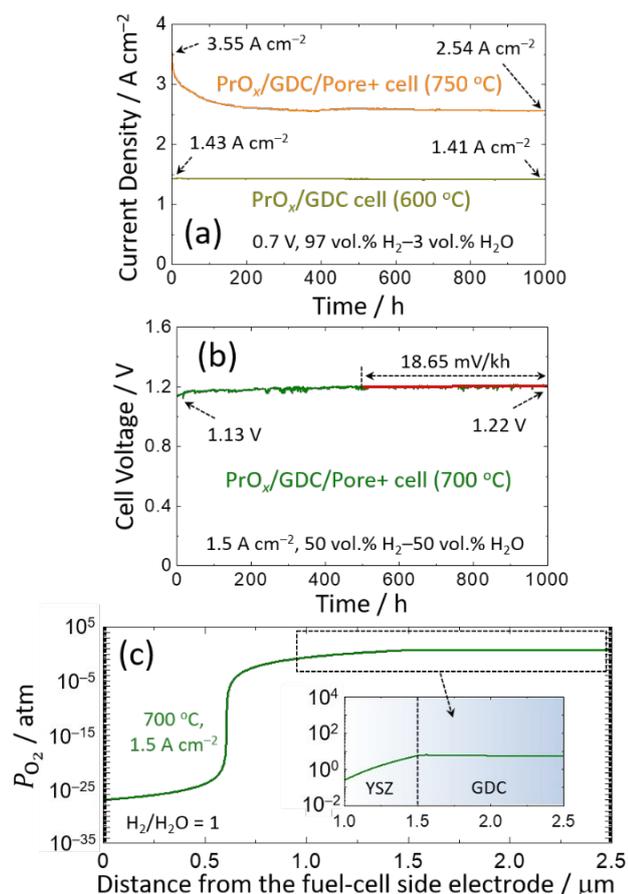

Fig. 7 (a) Evolution of current density with time during fuel cell life tests at 0.7 V in 97 vol.% H$_2$–3 vol.% H$_2$O and air for the PrO$_x$/GDC at 600 °C and PrO$_x$/GDC/Pore+ cell at 750 °C. (b) Evolution of cell voltage with time for the PrO$_x$/GDC/Pore+ cell during an electrolysis life test at 700 °C and 1.5 Acm^{-2} in 50 vol.% H$_2$–50 vol.% H$_2$O and air. (c) The calculated oxygen partial pressure (P_{O_2}) vs. position in the electrolyte of the PrO$_x$/GDC/Pore+ cell under the life test conditions in (b).

3. Conclusions

The main conclusions can be summarized as follows:

1. Solid oxide cells with unprecedented high performance – e.g., area specific resistance, ~0.1 Ωcm², fuel cell power density ~3 Wcm⁻², and electrolysis current density ~4 Acm⁻

2. – can be achieved by tuning the materials and microstructures of each of the main cell components;

2. Key cell features that are important for achieving high performance include an ~2.5 μm-thick GDC/YSZ bi-layer electrolyte, Ni–YSZ cell support with enhanced porosity, and electrode surface modification using PrO$_x$ and GDC nanocatalysts.

3. The support porosity is particularly important to minimize concentration polarization at higher operating temperature and in electrolysis operation due to the relatively low diffusivity of H$_2$O.

4. Subtraction of impedance spectra is used to help determine how rate-limiting electrode processes are impacted by the above modifications.

5. Besides showing exceptionally high performance, fuel cell and electrolysis life tests suggest very promising long-term stability in fuel cell and steam electrolysis mode.

4. Experimental

4.1 Cell fabrication

STFC was produced via solid state reaction as reported elsewhere.[18,34] The resultant STFC powders were mixed with vehicle (V-737, Heraeus) in a weight ratio of 1:1.2 in a three-roll mill to prepare the screen-printing paste. The NiO–YSZ-supported half-cells were produced by tape casting and lamination using 45 wt.% NiO–45 wt.% YSZ–10 wt.% starch (support layer), 50 wt.% NiO–50 wt.% YSZ (electrode functional layer), and YSZ with 1 mol.% Fe$_2$O$_3$ sintering aid (electrolyte layer). For PrO$_x$/GDC/Pore+ cells, the porosity of the support layer was improved by adding additional graphite pore former, with the composition 39 wt.% NiO–39 wt.% YSZ–10 wt.% starch–12 wt.% graphite. The increased porosity decreased the strength of the cells, but it was still sufficient for handling and to allow extended life testing; however, the trade-off between porosity and strength must be considered in the development of larger-area cells and stacks. The tape casting blade gap was carefully controlled to obtain the desired thicknesses. After lamination of these layers and pre-sintering at 1150 °C for 2 h, the 3 mol.% Fe$_2$O$_3$-doped GDC layers were formed onto the YSZ surfaces by dip-coating, followed by co-sintering at 1250 °C for 4 h. Note that the Fe$_2$O$_3$ (Alfa Aesar, 99.8 %) were used as a sintering aid with the amount chosen to obtain a high density bi-layer electrolyte by firing at 1250 °C.[16] The STFC oxygen electrodes (active area: 0.5 cm²) were formed via screen-printing onto the GDC diffusion barrier layer of the half-cell. After firing at 1050 °C for 3 h, the STFC electrode was found to be ~8 μm thick.

4.2 PrO$_x$ and GDC infiltration

For the single-step infiltration, aqueous nitrate solutions of PrO$_x$ or GDC precursors of 1 mol L⁻¹ were prepared by dissolving desirable amounts of Pr(NO$_3$)$_3$·6H$_2$O, Gd(NO$_3$)$_3$·6H$_2$O and Ce(NO$_3$)$_3$·6H$_2$O in distilled water. Triton X-100 and citric acid were additionally added into the precursor solution as a surfactant and a chelating agent, respectively. Selected

cathodes were infiltrated with 2 µL of PrO$_x$ solution. The cells were then mounted/sealed on alumina tubes using silver paste (DAD-87, Shanghai Research Institute of Synthetic Resins), and then mounted in the cell test stand. The cells were then heated to 550 °C for ~3 h to calcine the oxygen electrodes; the fuel electrodes were exposed to reducing atmospheres during this procedure in order to reduce the NiO in the electrodes to Ni (Fig. S15). After cooling and removal of the cell (together with a short section of the support tube) from the test setup, Ni–YSZ electrodes in selected cells were infiltrated with 10 µl of GDC solution. Finally, the cells were re-inserted into the test setup and the infiltrated material converted to GDC by in-situ thermal conversion during the SOC startup.

4.3 Electrochemical characterization

Silver grids (Heraeus) were screen-printed on the oxygen electrodes for current collection. All NiO–YSZ supported SOCs produced here underwent a specific startup procedure where initial heating to 600 °C was done in Ar and then the amount of hydrogen was gradually increased (Fig. S15). When a standard heatup in hydrogen was employed, cell OCV values were often low and erratic, suggesting that that mechanical stresses during NiO reduction lead the formation of micro-cracks across the very thin electrolyte. The oxygen and fuel electrodes were fed with air (500 sccm) and 3 vol.% H_2O-humidified H_2 (100 sccm) during fuel cell testing; whereas 50 vol.% H_2O was employed during electrolysis testing. The electrochemical characterization was carried out with an IM6 Electrochemical Workstation (ZAHNER) at 550–800 °C. The EIS data were collected under open circuit conditions by using a 20 mV ac signal in the frequency range of from 0.1 Hz to 100 kHz. Simulation of the impedance data and complex nonlinear least squares fitting of the equivalent circuit models to the data was performed using a software programmed in Python that relies on the scientific Python stack.[50-53] The library mpmath was used to provide higher precision complex floating-point arithmetic.[54]

4.4 Materials characterization

The microstructural observation and surface chemistry were performed on the post-test cells through scanning electron microscopy (SEM, Hitachi S-4800) combined with energy-dispersive X-ray spectroscopy (EDS, Oxford INCA).

Conflicts of interest

There are no conflicts to declare.

Acknowledgements

References

1   J. B. Hansen, *Faraday Discuss.*, 2015, **182**, 9-48.
2   M. B. Mogensen, M. Chen, H. L. Frandsen, C. Graves, J. B. Hansen, K. V. Hansen, A. Hauch, T. Jacobsen, S. H. Jensen, T. L. Skafte and X. Sun, *Clean Energy*, 2019, **3**, 175-201.
3   Z. Gao, L. V. Mogni, E. C. Miller, J. G. Railsback and S. A. Barnett, *Energy Environ. Sci.*, 2016, **9**, 1602-1644.
4   J. E. O'Brien, M. G. McKellar, E. A. Harvego and C. M. Stoots, *Int. J. Hydrogen Energy*, 2010, **35**, 4808-4819.
5   P. Iora, P. Chiesa and S. Campanari, *Energy Procedia*, 2014, **61**, 639-642.
6   R. Küngas, P. Blennow, T. Heiredal-Clausen, T. Holt, J. Rass-Hansen, S. Primdahl and J. B. Hansen, *ECS Trans.*, 2017, **78**, 2879-2884.
7   N. Xu, X. Li, X. Zhao, J. B. Goodenough and K. Huang, *Energy Environ. Sci.*, 2011, **4**, 4942-4946.
8   C. Graves, S. D. Ebbesen, S. H. Jensen, S. B. Simonsen and M. B. Mogensen, *Nat. Mater.*, 2014, **14**, 239.
9   S. H. Jensen, C. Graves, M. Mogensen, C. Wendel, R. Braun, G. Hughes, Z. Gao and S. A. Barnett, *Energy Environ. Sci.*, 2015, **8**, 2471-2479.
10 D. M. Bierschenk, J. R. Wilson and S. A. Barnett, *Energy Environ. Sci.*, 2011, **4**, 944-951.
11 C. H. Wendel, Z. Gao, S. A. Barnett and R. J. Braun, *J. Power Sources*, 2015, **283**, 329-342.
12 J. Graetz, *Chem. Soc. Rev.*, 2009, **38**, 73-82.
13 E. Tzimas, P. Castello and S. Peteves, *Int. J. Hydrogen Energy*, 2007, **32**, 1369-1380.
14 E. D. Wachsman and K. T. Lee, *Science*, 2011, **334**, 935-939.
15 G. Botta, R. Mor, H. Patel and P. V. Aravind, *Appl. Energy*, 2018, **226**, 1100-1118.
16 Z. Gao, V. Y. Zenou, D. Kennouche, L. Marks and S. A. Barnett, *J. Mater. Chem. A*, 2015, **3**, 9955-9964.
17 J. Schefold, A. Brisse and F. Tietz, *J. Electrochem. Soc.*, 2012, **159**, A137-A144.
18 S.-L. Zhang, H. Wang, M. Y. Lu, A.-P. Zhang, L. V. Mogni, Q. Liu, C.-X. Li, C.-J. Li and S. A. Barnett, *Energy Environ. Sci.*, 2018, **11**, 1870-1879.
19 Z. Yang, J. Zhang, M. C. W. Kintner-Meyer, X. Lu, D. Choi, J. P. Lemmon and J. Liu, *Chem. Rev.*, 2011, **111**, 3577-3613.
20 M. Powell, K. Meinhardt, V. Sprenkle, L. Chick and G. McVay, *J. Power Sources*, 2012, **205**, 377-384.
21 H.-S. Noh, K. J. Yoon, B.-K. Kim, H.-J. Je, H.-W. Lee, J.-H. Lee and J.-W. Son, *J. Power Sources*, 2014, **247**, 105-111.
22 J. Kim, S. Sengodan, G. Kwon, D. Ding, J. Shin, M. Liu and G. Kim, *ChemSusChem*, 2014, **7**, 2811-2815.
23 Z. Gao, H. Wang, E. Miller, Q. Liu, D. Senn and S. Barnett, *ACS Appl. Mater. Interfaces*, 2017, **9**, 7115-7124.
24 S. Choi, C. J. Kucharczyk, Y. Liang, X. Zhang, I. Takeuchi, H.-I. Ji and S. M. Haile, *Nat. Energy*, 2018, **3**, 202-210.

25 K. J. Yoon, M. Biswas, H.-J. Kim, M. Park, J. Hong, H. Kim, J.-W. Son, J.-H. Lee, B.-K. Kim and H.-W. Lee, *Nano Energy*, 2017, **36**, 9-20.

26 A. Chrzan, S. Ovtar, P. Jasinski, M. Chen and A. Hauch, *J. Power Sources*, 2017, **353**, 67-76.

27 Y. Lu, P. Gasper, U. B. Pal, S. Gopalan and S. N. Basu, *J. Power Sources*, 2018, **396**, 257-264.

28 A. V. Call, J. G. Railsback, H. Wang and S. A. Barnett, *Phys. Chem. Chem. Phys.*, 2016, **18**, 13216-13222.

29 C. Kim, J. Kim, J. Shin and G. Kim, *Int. J. Hydrogen Energy*, 2014, **39**, 20812-20818.

30 S. Choi, T. C. Davenport and S. M. Haile, *Energy Environ. Sci.*, 2019, **12**, 206-215.

31 J. Kim, A. Jun, O. Gwon, S. Yoo, M. Liu, J. Shin, T.-H. Lim and G. Kim, *Nano Energy*, 2018, **44**, 121-126.

32 W. Li, B. Guan, L. Ma, S. Hu, N. Zhang and X. Liu, *J. Mater. Chem. A*, 2018, **6**, 18057-18066.

33 D. Huan, N. Shi, L. Zhang, W. Tan, Y. Xie, W. Wang, C. Xia, R. Peng and Y. Lu, *ACS Appl. Mater. Interfaces*, 2018, **10**, 1761-1770.

34 M. Y. Lu, R. Scipioni, B.-K. Park, T. Yang, Y. A. Chart and S. A. Barnett, *Mater. Today Energy*, 2019, **14**, 100362.

35 B.-K. Park, R. Scipioni, D. Cox, S. A. Barnett, *J. Mater. Chem. A*, 2020, **8**, 4099-4106.

36 C. Nicollet, A. Flura, V. Vibhu, A. Rougier, J.-M. Bassat and J.-C. Grenier, *Int. J. Hydrogen Energy*, 2016, **41**, 15538-15544.

37 S. Ovtar, X. Tong, J. J. Bentzen, K. T. S. Thydén, S. B. Simonsen and M. Chen, *Nanoscale*, 2019, **11**, 4394-4406.

38 J. R. Wilson and S. A. Barnett, *Electrochem. Solid-State Lett.*, 2008, **11**, B181-B185.

39 T. Chen, Y. Zhou, M. Liu, C. Yuan, X. Ye, Z. Zhan and S. Wang, *Electrochem. Commun.*, 2015, **54**, 23-27.

40 H. Sun, Y. Chen, F. Chen, Y. Zhang and M. Liu, *J. Power Sources*, 2016, **301**, 199-203.

41 S. H. Jensen, A. Hauch, P. V. Hendriksen, M. Mogensen, N. Bonanos and T. Jacobsen, *J. Electrochem. Soc.*, 2007, **154**, B1325-B1330.

42 T. Ramos, M. Søgaard and M. B. Mogensen, *J. Electrochem. Soc.*, 2014, **161**, F434-F444.

43 A. Leonide, V. Sonn, A. Weber and E. Ivers-Tiffée, *J. Electrochem. Soc.*, 2008, **155**, B36-B41.

44 M. Shah, P. W. Voorhees and S. A. Barnett, *Solid State Ionics*, 2011, **187**, 64-67.

45 Y. Zhang, M. Ni, M. Yan and F. Chen, *J. Power Sources*, 2015, **299**, 578-586.

46 B.-K. Park, Q. Zhang, P. W. Voorhees and S. A. Barnett, *Energy Environ. Sci.*, 2019, **12**, 3053-3062.

47 M. Chen, Y.-L. Liu, J. J. Bentzen, W. Zhang, X. Sun, A. Hauch, Y. Tao, J. R. Bowen and P. V. Hendriksen, *J. Electrochem. Soc.*, 2013, **160**, F883-F891.

48 R. Knibbe, M. L. Traulsen, A. Hauch, S. D. Ebbesen and M. Mogensen, *J. Electrochem. Soc.*, 2010, **157**, B1209-B1217.

49 Q. Liu, Q. Zhang, P. W. Voorhees and S. A. Barnett, *J. Phys.: Energy*, 2019, **2**, 014006.

50 C. Graves, RAVDAV Data Analysis Software v. 0.9.7, 2012.

51 E. Jones, T. Oliphant and P. Peterson, P. SciPy: Open Source Scientific Tools for Python, 2001.

52 S. v. d. Walt, S. C. Colbert and G. Varoquaux, *Comput. Sci. Eng.*, 2011, **13**, 22-30.

53 J. D. Hunter, *Comput. Sci. Eng.*, 2007, **9**, 90-95.

54 F. Johansson, *ACM Commun. Comput. Algebra*, 2014, **47**, 166-169.

Tuning electrochemical and transport processes to achieve extreme performance and efficiency in solid oxide cells
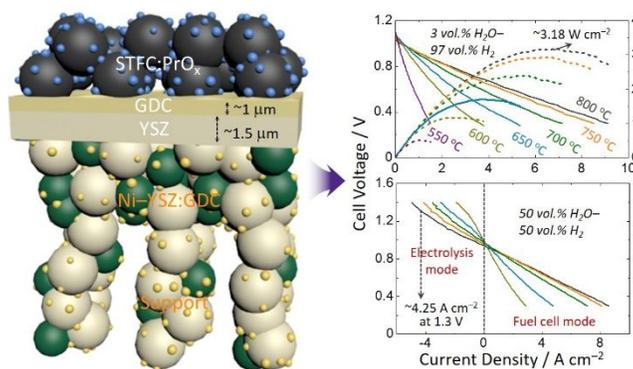
Beom-Kyeong Park, Roberto Scipioni, Qian Zhang, Dalton Cox, Peter W. Voorhees, and Scott

A. Barnett *

Department of Materials Science and Engineering, Northwestern University, Evanston, Illinois 60208, USA

* Corresponding author

E-mail: s-barnett@northwestern.edu

A new SOC that utilizes a very thin GDC/YSZ bi-layer electrolyte, support with enhanced porosity, and electrode surface modification *via* PrO_x and GDC nanocatalysts pushes the limits of cell polarizations, exceeding fuel cell power density ~3 Wcm^{-2} and electrolysis current density ~4 Acm^{-2}.